1

Pressure-Induced sp^2-sp^3 Transitions in Carbon-Bearing Phases

Sergey S. Lobanov[1] and Alexander F. Goncharov[2]

ABSTRACT

Carbon-bearing phases show a rich variety of structural transitions as an adaptation to pressure. Of particular interest is the crossover from sp^2 carbon to sp^3 carbon, as physical and chemical properties of carbon in these distinct electronic configurations are very different. In this chapter we review pressure-induced sp^2-sp^3 transitions in elemental carbon, carbonates, and hydrocarbons.

1.1. INTRODUCTION

Understanding of pressure-induced phase transitions in carbon-bearing phases is fundamental for physics and chemistry of dense condensed matter and has important implications for Earth and planetary sciences. Carbon is unique in that it can form compounds with three distinct electronic configurations (we will focus on sp^2 and sp^3 configurations here) depending on the way *s* and *p* atomic orbitals of carbon interact with each other. The different geometrical arrangement of chemical bonds typical of compounds with sp^2-bonded and sp^3-bonded carbon (Figure 1.1, inset) results in threefold (lower steric repulsion) and fourfold (higher steric repulsion) coordination, respectively. High pressure is an efficient driver for sp^2-sp^3 transitions as it promotes denser crystal structures and allows negating the steric repulsion of neighboring atoms in sp^3 phases. More often than not, material properties over such transitions change in a radical manner. It is most obvious in the case of pure carbon where graphite and diamond represent archetypal examples of sp^2-bonded and sp^3-bonded crystals, which are extremely dissimilar in the crystal and electronic structure, and hence in the properties such as, for example, electrical conductivity, elasticity, and vibrational anisotropy (Oganov et al., 2013).

[1] *GFZ German Research Center for Geosciences, Potsdam, Germany*

[2] *Geophysical Laboratory, Carnegie Institution for Science, Washington, DC, USA*

Carbon prefers the sp^2-configuration at low pressure, although there are exceptions (e.g. CH_4), because of the small carbon atomic radius (70 pm) that is not sufficient to reduce steric repulsion among the atoms in its coordination. The increase of coordination number upon the sp^2-sp^3 transition always entails longer carbon-to-neighbor bonds in the sp^3-phase to compensate for the increase in steric repulsion (Prewitt & Downs, 1998). As a result, significant atomic rearrangements are necessary for sp^2-sp^3 phase transitions with large energy barriers typical of such crossovers (Powles et al., 2013). High-temperature (*T*) conditions are often required to reach the thermodynamic ground state, such as in the case of graphite and diamond. Consequently, many carbon-bearing phases can be preserved outside their thermodynamic stability range. This intrinsic metastability of sp^3 carbons finds many useful scientific and technological applications. Natural diamonds, despite being metastable at ambient conditions, often secure unique samples of the Earth's mantle due to their chemical inertness (Kopylova et al., 2010; Wirth et al., 2014; Pearson et al., 2014; Smith et al., 2016; Nestola et al., 2018; Tschauner et al., 2018). The sluggish kinetics of the graphite-to-diamond transition also helps to decipher the complex *P*-*T* history of high-pressure metamorphic complexes and mantle xenoliths (De Corte et al., 2000; Hwang et al., 2001; Massonne, 2003; Korsakov et al., 2010; Mikhailenko et al., 2016; Shchepetova et al., 2017). The rich polymorphism of carbonates driven by the diverse carbon bonding patterns presents another example with relevance to geosciences as it creates

Carbon in Earth's Interior, Geophysical Monograph 249, First Edition. Edited by Craig E. Manning, Jung-Fu Lin, and Wendy L. Mao.

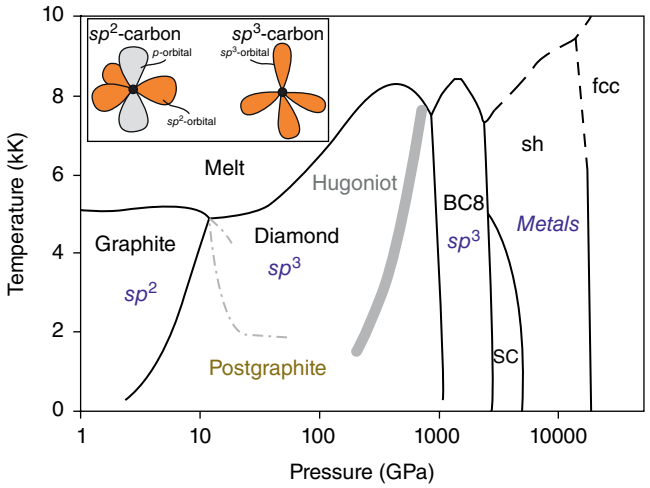

Figure 1.1 Phase diagram of carbon at extreme *P-T* conditions. BC8, sc (simple cubic), sh (simple hexagonal), and fcc (face-centered cubic) are theoretically predicted carbon structures at $P > 1$ TPa that have never been observed in experiment. Inset: The electronic structure of sp^2 and sp^3-hybridized carbon. See electronic version for color representation of the figures in this book.

pathways for transporting carbon into the deep mantle. Aside from the geological importance, the sp^2-sp^3 polymorphism of carbon-bearing phases is of great technological interest as it allows accessing a rich range of diverse physical and chemical properties in an isochemical setting (Field, 1992). This chapter reviews sp^2-sp^3 transitions in carbon-bearing phases that include pure carbon, carbonates, and hydrocarbons.

1.2. ELEMENTAL CARBON

Graphite and diamond are the only two stable allotropes of carbon at $P < \sim$1000 GPa (Figure 1.1). However, a variety of metastable phases are known with a broad range of kinetic stability, which is a unique feature of carbon, making its phase diagram very complex, especially at near-ambient conditions (e.g. Bundy et al., 1996). In addition, the melting curves of the carbon polymorphs remain uncertain in the limit of high pressure and high temperature, where obtaining direct experimental data is challenging. Here we update the previous reviews (Oganov et al., 2013; Bundy et al., 1996; Goncharov, 1987; Hazen et al., 2013), mainly concentrating on the phase relations at extreme conditions and focusing on materials of interest to geosciences.

1.2.1. Metastable Phases

Lonsdaleite is a naturally occurring diamond polytype that was first described in Canyon Diablo meteorite (Frondel & Marvin, 1967; Hanneman et al., 1967) and has been used since to pinpoint the *P-T* conditions of the impact. Lonsdaleite has a hexagonal crystal structure that has a slightly higher energy than cubic diamond. As such, the formation of this phase (e.g. from graphite) must follow a certain kinetic route (Erskine & Nellis, 1991; Xie et al., 2017; Bundy & Kasper, 1967), making its occurrence difficult to uniquely identify in both natural and synthetic samples. This resulted in conflicting reports concerning the microstructure of samples synthesized at static pressure conditions, questioning the uniqueness of lonsdaleite as a structurally discrete material (Németh et al., 2014; Shiell et al., 2016). Further, the existence of a nanometer (nm) scale structural complexity in lonsdaleite makes its characterization complex even at ambient conditions. As a result of its structural complexities, the mechanism of lonsdaleite formation in early shock wave experiments (e.g. Erskine & Nellis, 1991) was difficult to resolve. In recent years, however, the development of in situ X-ray diffraction (XRD) characterization of dynamic processes on a very fast time scale (ps to ns) allowed for better understanding of the lonsdaleite formation and the carbon phase diagram (Rygg et al., 2012; Gupta et al., 2012; Gauthier et al., 2014). Nevertheless, ambiguities still exist. For example, a direct transition from graphite to lonsdaleite at 50 GPa was inferred by Turneaure et al. (2017), while Kraus et al. (2016) reported on a different sequence that includes a transition to cubic diamond at 50 GPa and subsequently to lonsdaleite at 170 GPa. These works stimulate the development of theoretical models, which also remain contradictory concerning the mechanisms of graphite-to-diamond transformations (Xie et al., 2017; Pineau, 2013; Mundy et al., 2008; Khaliullin et al., 2011).

As with lonsdaleite, other metastable carbon phases may serve as indicators of shock metamorphism *P-T* conditions. Several kinetically accessible carbon materials are formed by compression of graphite (and other metastable sp^2-bonded carbons) at room temperature. Without sufficient thermal energy to activate the transition to diamond-like phases, the system relaxes in structures that represent a compromise between the thermodynamic stimulus and kinetic hindrance. Cold compression (at 300 K) to above 15 GPa, well into the stability field of diamond, results in an sp^3-bonded form of carbon (termed postgraphite here) as suggested by a decrease in the electrical conductivity, appearance of optical transparency, and changes in inelastic X-ray scattering spectra (Goncharov et al., 1989; Utsumi & Yagi, 1991; Mao et al., 2003). XRD measurements on this sp^3-bearing carbon are not conclusive in the structural determination (Mao et al., 2003; Wang et al., 2012) because only powder-like data was examined and the peaks of the high-pressure phase were weak and broad. Raman spectroscopy, which is generally sensitive to the

type of chemical bonding, is also not decisive as sp^3 carbon has a two orders of magnitude smaller scattering cross-section compared to sp^2 carbon when the spectra are excited in the visible spectral range (Ferrari, 2002). The Raman spectra of cold-compressed graphite (Wang et al., 2012; Goncharov et al., 1990; Xu et al., 2002) show a large broadening of the C-C stretching mode of the sp^2-bonded carbon in the high-pressure phase. However, positive spectroscopic identification of sp^3-bonded carbon has not been achieved because the first-order diamond peak of the diamond anvils and the disorder-induced D-band of sp^2-bonded carbon both obscure the spectral range of interest. Overall, the XRD and Raman data suggest the presence of disorder in postgraphite phase(s). The persistence of the sp^2 fingerprints in its Raman spectra upon cold compression indicates that postgraphite still contains sp^2-bonded carbon, which is inconsistent with the theoretically predicted M-carbon phase (Li et al., 2009) usually considered the best match to the experiment. Interestingly, the transition to postgraphite is reversible at 300 K (Utsumi & Yagi, 1991; Mao et al., 2003; Wang et al., 2012), but this phase can be quenched at low temperatures <100 K (Miller et al., 1997). A very similar phase can be obtained from carbon nanotubes (albeit at higher pressures than from graphite), which appears quenchable to ambient conditions (Wang et al., 2004).

Annealing of a cold-compressed graphite at T >1000 K and P ~20 GPa results in a pressure-quenchable phase that is structurally different from postgraphite and shows similarities to lonsdaleite (Utsumi & Yagi, 1991). Glassy carbon cold-compressed to 50 GPa and heated to ~1800 K produces an amorphous and pressure-quenchable sp^3-bonded phase (Zeng et al., 2017; Yin et al., 2011). These results highlight the importance of the initial carbon microstructure on the dense high-pressure synthesis products, which has the potential for creating new ultralight and ultrastrong materials (Hu et al., 2017). Theoretical description of all these metastable carbon phases (see Shi et al., 2018, and references therein) remains largely unsatisfactory.

1.2.2. Phase Diagram at High Temperature and in the TPa Pressure Range

In the limit of high temperature, the graphite-to-diamond transition is well established and sharp (Bundy et al., 1996). In contrast, the theoretically predicted sp^2-sp^3 transition in molten carbon is sluggish and the results appear sensitive to the level of theory used in the computation (e.g. first-principles vs. classical) (Ghiringhelli et al., 2004). With regard to solid–solid transformations and melting at very high pressures, carbon is unique in the group IV of the periodic table in that it has no p-electrons in the core, allowing the valence p-electrons to be closer to the nucleus, making stronger directional chemical bonds (Yin & Cohen, 1983). As a result, the diamond structure has a much larger P-T stability range compared to its Si and Ge sp^3 analogs. Unlike Si and Ge, the melting curve of diamond is positive (above the graphite-diamond-melt triple point) (Bundy et al., 1996), and the sp^3-bonded BC8 phase stable at P > ~1 TPa is not metallic (cf. β-tin Si) but semiconducting (Correa et al., 2006; Martinez-Canales et al., 2012). According to theoretical calculations (Wang et al., 2005; Benedict et al., 2014), the slope of this diamond melting curve changes from positive to negative above 450 GPa due to the softening of the transverse acoustic branches near the L and X symmetry points (Correa et al. 2006). Dynamic compression experiments detected the melting of diamond close to the expected range of P-T conditions, inferred a crossover in the slope of its melting line, and provided evidence of the second diamond-BC8-liquid triple point (Brygoo et al., 2007; Knudson et al., 2008; Eggert et al., 2009). At higher pressures, theory predicts that the BC8 structure undergoes metallization (Correa et al., 2006) or transforms to a metallic simple cubic (sc) phase above 2.7 TPa, and then further to metallic simple hexagonal (sh) and cubic fcc structures (Figure 1.1) (Martinez-Canales et al., 2012; Benedict et al., 2014). Recent ramp compression experiments that relied on single-surface velocity measurements did not record discontinuities that could be attributed to the predicted phase transition (Smith et al., 2014). In the absence of direct structural characterization, however, any robust conclusion seems premature.

1.3. CARBONATES

1.3.1. (Mg,Fe) Carbonates

To the best of our knowledge, Skorodumova et al. (2005) provided the first computational evidence of thermodynamic stability of sp^3-$MgCO_3$ with a pyroxene structure ($C2/c$) at P > 113 GPa with CO_4^{2-} tetrahedral groups arranged in chains. This study, however, explored only the relative stabilities of several possible sp^3-carbonate structures as suggested by crystallographic and chemical similarities with Mg-bearing silicates. The first unconstrained search for the stable structures in the $MgCO_3$ system by evolutionary crystal structure prediction algorithms revealed an sp^2-sp^3 transition at 82 GPa (Oganov et al., 2008) with a $C2/m$ structure being ~0.2 eV more favorable than the pyroxene structure initially proposed by Skorodumova et al. (2005). This sp^3-$MgCO_3$ phase was termed magnesite-II (phase II) with a wide stability field up to 138 GPa where another sp^3 modification of $MgCO_3$ ($P2_1$, phase III) was predicted to take over (Oganov et al., 2008). More structures, however, were

proposed in the 90–120 GPa range as energetically competitive by Panero and Kabbes (2008) based on a first principles evaluation of several potential structures. Pickard and Needs (2015) revised the phase diagram of $MgCO_3$ using ab initio random structure searching technique to find new stable *P*-1 (85-101 GPa) and $P2_12_12_1$ (*P* >144 GPa) $MgCO_3$ structures with sp^3 carbon in addition to the *C*2/*m* structure proposed earlier (Oganov et al., 2008). Most recently, another polymorph of sp^3-$MgCO_3$ ($P2_1$) was predicted at *P* > 143 GPa (Yao et al., 2018). Figure 1.2 summarizes theoretical predictions for the $MgCO_3$ (and other) system(s).

These first-principles predictions stimulated the experimental search for pressure-induced sp^2-sp^3 transitions in carbonates. Boulard et al. (2011) attempted to synthesize sp^3-$MgCO_3$ in a diamond anvil cell (DAC) using synchrotron XRD as a probe to detect the new phases. At 80 GPa and ~2400 K, the authors observed new XRD peaks that could not be attributed to the starting materials ($MgCO_3$ or MgO + CO_2). This new phase was not temperature-quenchable and only the low-pressure magnesite structure could be observed after cooling (Boulard et al., 2011). Nonetheless, on the basis of Le Bail–type crystallographic refinement of high-temperature XRD patterns, the authors concluded that they successfully synthesized magnesite II with a crystal structure based on three CO_4-tetrahedra linked into $(C_3O_9)^{6-}$ rings

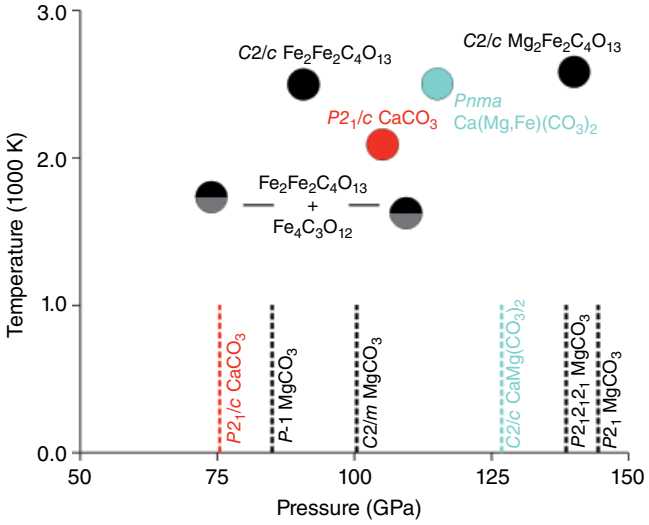

Figure 1.2 Pressure-temperature conditions of sp^2-sp^3 phase transitions in carbonates. Theoretical predictions (calculations at 0 K) are shown by dashed lines. Only the most recent reports are shown: $MgCO_3$ (Pickard & Needs, 2015; Yao et al., 2018), $CaMg(CO_3)_2$ (Solomatova & Asimow, 2017), and $CaCO_3$ (Pickard & Needs, 2015). Circles depict the synthesis conditions of sp^3-phases in (Mg,Fe)- (Merlini et al., 2015), (Ca,Mg,Fe)- (Merlini et al., 2017), and Ca-carbonate (Lobanov et al., 2017) systems. See electronic version for color representation of the figures in this book.

(Boulard et al., 2011). A crystal structure with $P2_1/c$ symmetry allowed for improved Le Bail refinement over the predicted *C*2/*m* $MgCO_3$ structure.

Similar experimental evidence was put forward in support of the sp^3-(Fe, Mg)CO_3 synthesis from $(Fe_{0.75}Mg_{0.25})$ CO_3 or $(Mg_{0.6}Fe_{0.4})$ + CO_2 after laser heating to ~2000 K at 80 GPa and to ~2850 K at 105 GPa, respectively (Boulard et al., 2011). Regardless of the starting components, the measured XRD patterns showed similarities to that observed in pure $MgCO_3$, and the authors concluded that the same crystal structure formed in these two systems. In the iron-containing system, however, the synthesized phase was not only temperature-quenchable but also pressure-quenchable, and the recovered samples were analyzed by electron energy loss spectroscopy, which showed a peak at 290.7 eV (assigned to $C_3O_9^{6-}$) as opposed to 290.3 eV in reference sp^2-siderite (Boulard et al., 2011). However, it is unclear whether the authors' interpretation is unequivocal as the reported energy resolution (width of the zero-loss peak at its half height) was 0.6 eV.

In a subsequent work, Boulard et al. (2015) reported on the room-temperature infrared spectrum of $(Fe_{0.75}Mg_{0.25})$ CO_3 that was presynthesized at ~2100 K at 103 GPa. The synthesis of *C*2/*m* (Fe,Mg)CO_3, as well as of a high-pressure polymorph of $CaMn_2O_4$-type Fe_3O_4, was reported based on synchrotron XRD. One should bear in mind, however, that reliable identification of these low symmetry structures at *P* ~100 GPa based solely on a Le Bail–type refinement is challenging. For example, the identification of the Fe_3O_4 structure could not have been possible because iron oxides show a complex high *P*-*T* behavior (Bykova et al., 2016), the details of which were not known at the time of the Boulard et al. (2015) work. The stable structure of Fe_3O_4 is different from the one used for Le Bail refinement in Boulard et al. (2015), which undermines the robustness and the overall conclusions of that work.

Merlini et al. (2015) provided a more reliable insight into the crystal structures of sp^3-(Fe,Mg) carbonates by means of single-crystal structure solution methods finding that sp^2-$(Fe_{0.75}Mg_{0.25})$ CO_3 transforms to a *C*2/*c* $Mg_2Fe_2(C_4O_{13})$ together with a *C*2/*m* $Fe_{13}O_{19}$ at *P* ~135 GPa and *T* ~2650 K (Figure 1.2). The new carbonate phase contained tetrahedrally coordinated sp^3-hybridized carbon linked into corner-shared truncated C_4O_{13} chains and apparently remained stable on decompression down to 40 GPa. Importantly, this study provided the first evidence that the composition of the (Mg,Fe) carbonate may change over the sp^2-sp^3 transition, which had not been considered by first-principles computations. A similar single-crystal XRD technique was subsequently applied to the $FeCO_3$ endmember uncovering two distinct sp^3 carbonates at *P* > ~70 GPa (Cerantola et al., 2017). According to this study, $Fe_4(C_3O_{12})$ and $Fe_2Fe_2(C_4O_{13})$ coexist in the temperature limit of ~1500–2200 K, while

only $Fe_2Fe_2(C_4O_{13})$ is present at T > ~2200 K. The crystal structure of $Fe_4(C_3O_{12})$ involves isolated CO_4 tetrahedra, while $Fe_2Fe_2(C_4O_{13})$ contains truncated chains of CO_4 tetrahedra (Figure 1.3) and is isostructural with $Mg_2Fe_2(C_4O_{13})$ found earlier by Merlini et al. (2015).

Overall, the case of (Mg,Fe) carbonates shows that they exhibit a remarkably complex crystallographic behavior over the sp^2-sp^3 transition. Initial theoretical predictions of the stable sp^3-$MgCO_3$ did find some experimental support in both Mg carbonates and (Mg,Fe) carbonates. However, subsequent advanced crystallographic studies of (Mg,Fe) carbonates and Fe carbonates unraveled a complex behavior that always involves a change in the carbonate chemical composition, which was not anticipated from the earlier ab initio computations. For these reasons, earlier experimental reports on sp^3-$(Mg,Fe)CO_3$ (Boulard et al., 2011, 2015, 2012) must be deemed unreliable.

1.3.2. Ca Carbonates and Ca(Mg,Fe) Carbonates

The theoretical search for an sp^2-sp^3 transition in $CaCO_3$ using evolutionary crystal structure prediction algorithms yielded an orthorhombic pyroxene-type ($C222_1$) structure at P > 137 GPa (Oganov et al., 2006). Ono et al. (2007) showed that laser-heating of $CaCO_3$ at P > 130 GPa results in a new phase that is structurally consistent with the predicted $C222_1$ $CaCO_3$. To the best of our knowledge, the synthesis of sp^3-$CaCO_3$ by Ono et al. (2007) is the first experimental report of an sp^3 carbonate. The crystal structure of this phase, however, was challenged by more recent computations that found that $P2_1/c$ $CaCO_3$ is ~0.2 eV/f.u. more energetically favorable than the $C222_1$ model and is stable at P > 76 GPa (Figure 1.2) and up to at least 160 GPa (Pickard & Needs, 2015; Yao et al., 2018). Both $C222_1$ and $P2_1/c$ $CaCO_3$ are based on CO_4-tetrahedra linked into 1D pyroxene-like chains with only slight differences in the arrangement of CO_4-groups. All vertex-sharing helices in the $C222_1$ structure are right-handed, while half helices in the $P2_1/c$ $CaCO_3$ are left-handed.

To test these theoretical predictions, Lobanov et al. (2017) used synchrotron XRD and Raman spectroscopy as probes for the sp^2-sp^3 transition. Crystallographic data collected after the heating of $CaCO_3$ to ~2000 K at 105 GPa provided evidence of the sp^2-sp^3 transition but were not sufficient to discriminate between the proposed $C222_1$ and $P2_1/c$ $CaCO_3$ models. Raman spectra measured before and after the heating, however, were clearly distinct. A characteristic C-O stretching vibration appears after the heating with a frequency that is ~20% lower than that in sp^2 $CaCO_3$ prior to the heating (Figure 1.4a), consistent with the longer C-O bond length in CO_4 tetrahedra. This spectral feature was reproduced independently via ab initio computations of the vibrational spectrum of sp^3 $CaCO_3$ and provided strong evidence in favor of the $P2_1/c$ model of $CaCO_3$ (Figure 1.4b). Altogether, the combined crystallographic and spectroscopic approach proved successful in detecting the sp^2-sp^3 transition in $CaCO_3$ and provided a reliable reference for the frequency of C-O stretching in CO_4 tetrahedra, which can be used to identify sp^2-sp^3 transitions in other carbonates (Lobanov et al., 2017).

Because of the chemical reactions with mantle minerals, $CaMg(CO_3)_2$ is a more realistic composition for the mantle carbonate. Merlini et al. (2017) reported on the synthesis of sp^3 $Ca(Mg_{0.6},Fe_{0.4})(CO_3)_2$ (dolomite-IV) at 115 GPa and 2500 K. The crystal structure of dolomite-IV was solved from single-crystal XRD data and contains CO_4 tetrahedra linked into threefold C_3O_9 rings

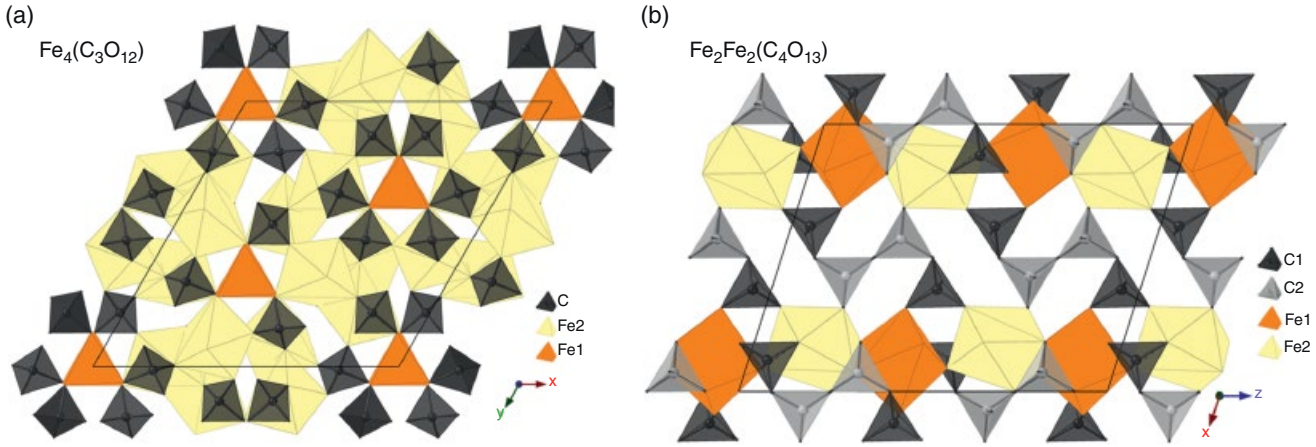

Figure 1.3 Crystal structures of $Fe_4(C_3O_{12})$ and $Fe_2Fe_2(C_4O_{13})$ after Cerantola, et al. (2017). Oxygen atoms are not shown for clarity. Unit cells are shown by thin black lines. See electronic version for color representation of the figures in this book.

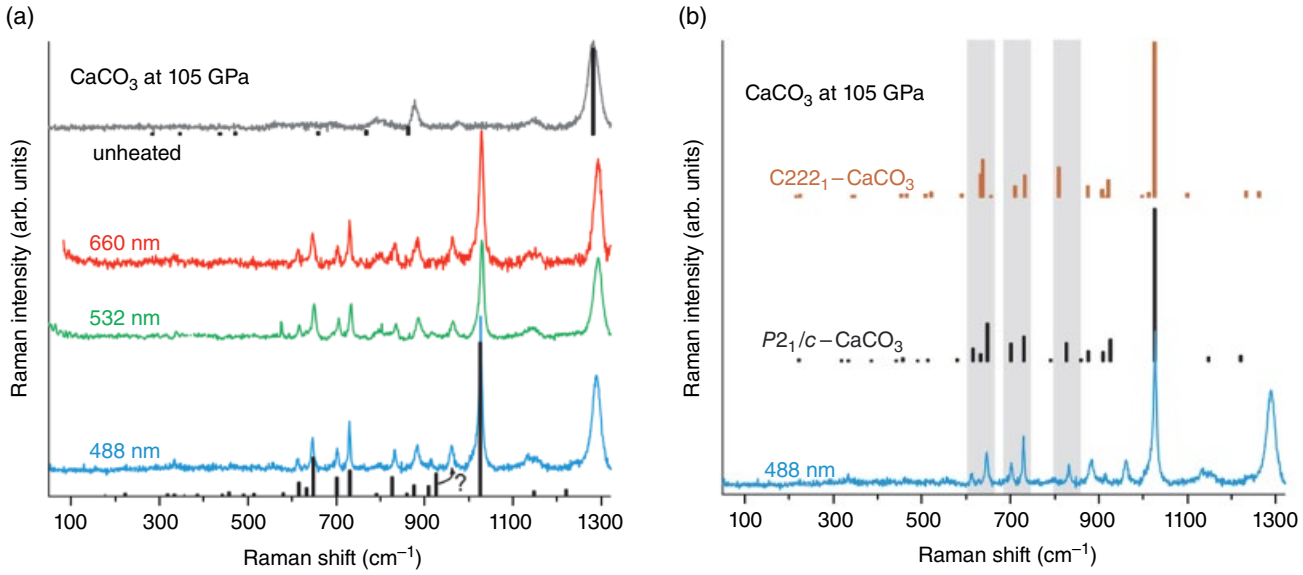

Figure 1.4 (a) Raman spectra of $CaCO_3$ at 105 GPa collected with 488, 532, and 660 nm excitations. Vertical bars are computed Raman modes of $P2_1/c$-$CaCO_3$ (bottom) and post-aragonite $CaCO_3$ (top). (b) Experimental spectrum of $CaCO_3$ laser-heated at 105 GPa in comparison with the theoretical spectra of $P2_1/c$ and $C222_1$-$CaCO_3$ at 105 GPa as computed by LDA-DFT. Shaded areas are guides to compare the computed spectra with experiment. Adapted from Lobanov et al., 2017. See electronic version for color representation of the figures in this book.

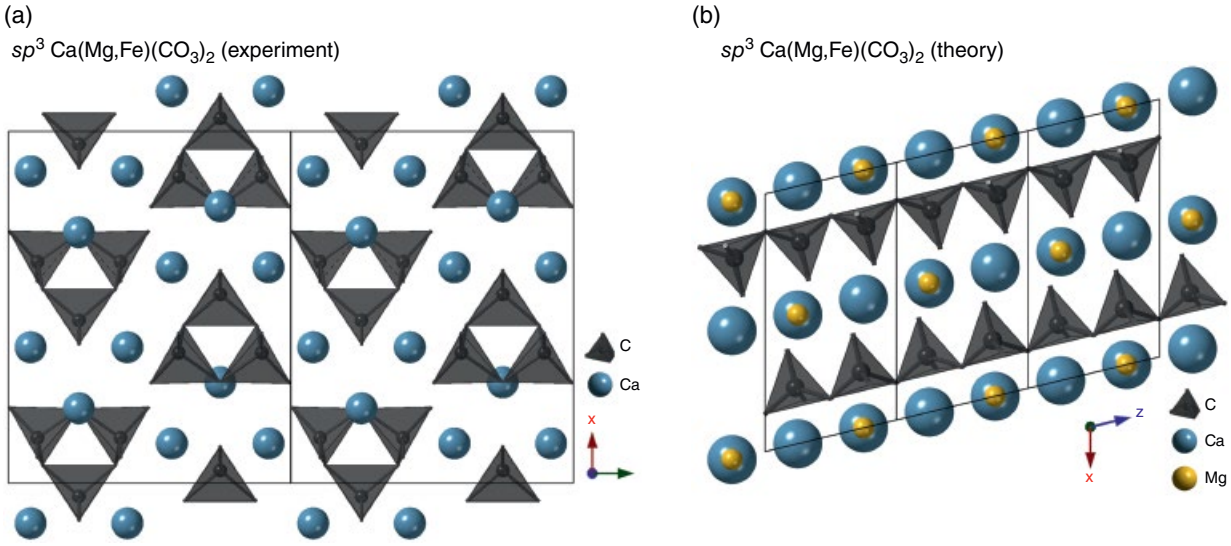

Figure 1.5 (a) Crystal structure of sp^3-$Ca(Mg_{0.6},Fe_{0.4})(CO_3)_2$ (dolomite-IV) after Merlini, et al. (2017). Mg and Fe atoms are not shown as they occupy identical crystallographic positions to Ca. (b) Theoretically predicted crystal structure of sp^3-$CaMg(CO_3)_2$ (Solomatova & Asimow, 2017). In a and b, oxygen atoms are not shown for clarity. Unit cells are shown by thin lines. See electronic version for color representation of the figures in this book.

(Figure 1.5a). Interestingly, Ca, Mg, and Fe cations occupy identical positions in the lattice, suggesting that moderate addition of iron does not bear important effects on the sp^3-$CaMg(CO_3)_2$ crystal structure. The presence of C_3O_9 rings in the dolomite-IV structure (Merlini et al., 2017) is an important similarity to the predicted magnesite-II phase (Oganov et al., 2008). However, an evolutionary search for sp^3-$CaMg(CO_3)_2$ yielded a different motif with CO_4-tetrahedra linked into pyroxene-like chains (Solomatova & Asimow, 2017), similarly to what has been predicted and experimentally confirmed for sp^3-$CaCO_3$. Interestingly, Raman spectra of dolomite-III at

P > 63 GPa, another polymorph of $CaMg(CO_3)_2$ stable at 36–115 GPa (Merlini et al., 2017), show a new band appearing as a low-frequency shoulder of the C-O symmetric stretching in CO_3 groups (Vennari & Williams, 2018). This shoulder was interpreted to be due to an increase in carbon coordination (3+1); thus, it may indicate a sluggish sp^2-sp^3 transition in $CaMg(CO_3)_2$ at room temperature.

In summary, $CaCO_3$ is the only sp^3 carbonate for which theoretical and experimental data on the structure of the sp^3-bonded phase are in agreement. The crystal structures of more complex sp^3 carbonates, such as in the (Mg,Fe) and (Ca,Mg) systems, have been solved directly from single crystal XRD data, but the agreement between these structures and those from theoretically predicted models is yet to be seen. Since the experimentally observed structures are chemically complex and contain a large number of atoms per cell, it is possible that earlier theoretical simulations on chemically simple carbonate systems did not sample unit cells with a sufficient number of atoms. On the other hand, it is possible that the experimentally observed phases are not representative of the ground state sp^3 structures because of severe chemical and thermal gradients that are typical of laser-heated DACs, especially when iron is present in the system. Subsequent studies employing multiple characterization techniques will be of significant value to the topic of sp^2-sp^3 transitions in carbonates.

1.4. HYDROCARBONS

High-pressure behavior of the carbon-hydrogen systems is relevant to planetary sciences as hydrocarbons are an important mantle component of icy giant planets (Hubbard, 1981). Application of high external pressure to hydrocarbons, which are typically soft molecular crystals, forces the molecules to shorten intermolecular distances, making intermolecular and intramolecular forces comparable (Hemley & Dera, 2000). At short enough intermolecular distances, molecules of unsaturated hydrocarbons (i.e. with π-bonds in the chemical structure) are forced to react with each other (polymerize) with the formation of conjugated molecular structures. Polymerization reactions in unsaturated hydrocarbons involve breaking of unsaturated π-bonds with the formation of σ-bonds between the adjacent molecules. As such, pressure-induced polymerization of unsaturated hydrocarbons can be viewed as an sp^2-sp^3 phase transition (Drickamer, 1967). This process is typically irreversible and hydrocarbon polymers are available for ex situ characterization after decompression.

Pressure-induced polymerization of unsaturated hydrocarbons has been extensively characterized by Raman and IR spectroscopy, which detected signatures of sp^3-bonded chemical structures at high pressure. Many examples of pressure-induced polymerization in unsaturated hydrocarbons have been reported in the literature (see Schettino & Bini, 2007, for a more thorough review). Below we provide only a handful of these. High-density polyethylene with a large fraction of sp^3 carbon can be obtained by compressing ethylene (C_2H_4) in a DAC at room temperature to ~3.6 GPa (Chelazzi et al., 2004). Solid acetylene polymerizes at 3.5 GPa with the *trans*-opening of the triple bond (Aoki et al., 1988; Santoro et al., 2003). Benzene, a prototype of aromatic compounds, polymerizes at P > 23 GPa (Prizan et al., 1990) with the formation of a one-dimensional sp^3 carbon nanomaterial (Fitzgibbons et al., 2015). Although the mechanism of benzene polymerization remains controversial (Wen et al., 2011), it is generally agreed that the process is governed by the pressure-activated π-π electron density overlap of the neighboring molecules, as initially suggested by Drickamer (1967). Ciabini et al. (2007) showed that benzene polymerization is triggered at a critical C-C distance of ~2.6 Å between adjacent C_6H_6 molecules. These experimentally observed polymerization reactions have also been reproduced by ab initio computations and confirm the importance of intermolecular separation and molecular orientation (Ciabini et al., 2007; Bernasconi et al., 1997).

The conjugated nature of the recovered products may give rise to peculiar physical properties. For example, a very high electrical conductivity (~100 Ω^{-1} cm^{-1}) was observed for polyacetylene (Clark & Hester, 1991). Hydrocarbons are expected to form polymeric states not only at relatively low pressures and room temperature but also at P-T conditions representative of planetary interiors (Lee & Scandolo, 2011; Chau et al., 2011; Sherman et al., 2012; Lobanov et al., 2013) where polymerized hydrocarbons may promote the high electrical conductivity expected of the icy mantles of Uranus and Neptune (Stanley & Bloxham, 2004). As such, knowledge of the conditions of hydrocarbon polymerization at extreme pressure and temperature is critical for our understanding of the icy giant planet interiors.

Many theoretical and experimental studies have explored the high P-T stability of hydrocarbons. Thermodynamic and molecular dynamics modeling of hydrocarbon systems showed that conjugated hydrocarbons (molecular and polymeric) are more stable at high pressure than at 1 atm (Sherman et al., 2012; Kenney et al., 2002; Zhang & Duan, 2009; Spanu et al., 2011; Gao et al., 2010). This is consistent with experimental reports on hydrocarbon synthesis from methane in laser-heated DACs (Lobanov et al., 2013; Hirai et al., 2009; Kolesnikov et al., 2009). Interestingly, unsaturated hydrocarbons can be formed from methane at P > 24 GPa and T > 1500 K (Lobanov et al., 2013), as observed by Raman spectroscopy at 300 K after laser heating. This, however, is inconsistent

with the apparent instability of unsaturated carbon-carbon double and triple bonds at high pressure (as discussed above). It is likely that Raman spectroscopy at 300 K provides a distorted snapshot of the hydrocarbon fluid at high temperature and that unsaturated carbon-carbon bonds form upon quenching of a highly dissociated fluid. Recent laser-shock experiments on hydrocarbons provided an in situ characterization of hydrocarbon fluids at high *P-T* and confirmed that such fluids are nonmolecular at $P < 100$–150 GPa and $T < \sim 3000$ K (Kraus et al., 2017). Further, this nonmolecular hydrocarbon fluid undergoes dissociation into diamond and hydrogen at $P > 150$ GPa and $T > 3000$ K. As such, methane dissociation to diamond and hydrogen at high *P-T* can be viewed as an sp^3-sp^3 transition.

ACKNOWLEDGMENTS

This work was supported by the Deep Carbon Observatory. SSL acknowledges the support of the Helmholtz Young Investigators Group CLEAR (VH-NG-1325) and Deutsche Forschungsgemeinschaft within the research group FOR2125 CarboPaT.

REFERENCES

Aoki, K., Usuba, S., Yoshida, M., Kakudate, Y., Tanaka, K., & Fujiwara, S. (1988). *J. Chem. Phys.*, *89*, 529.

Benedict, L. X., Driver, K. P., Hamel, S., Militzer, B., Qi, T. T., Correa, A. A., Saul, A., & Schwegler, E. (2014). *Phys. Rev. B*, *89*, 224109.

Bernasconi, M., Chiarotti, G. L., Focher, P., Parrinello, M., & Tosatti, E. (1997). *Phys. Rev. Lett.*, *78*, 2008.

Boulard, E., et al. (2012). *Journal of Geophysical Research*, *117*, B02208.

Boulard, E., Gloter, A., Corgne, A., Antonangeli, D., Auzende, A. L., Perrillat, J. P., Guyot, F., & Fiquet, G. (2011). *Proc. Natl. Acad. Sci. U.S.A.*, *108*, 5184.

Boulard, E., Pan, D., Galli, G., Liu, Z. X., & Mao, W. L. (2015). *Nature Comm.*, *6*, 6311.

Brygoo, S., Henry, E., Loubeyre, P., Eggert, J., Koenig, M., Loupias, B., Benuzzi-Mounaix, A., & Rabec Le Bundy, F. P., Bassett, W. A., Weathers, M. S., Hemley, R. J., Mao, H. U., & Goncharov, A. F. (1996). *Carbon*, *34*, 141.

Bundy, F. P., & Kasper, J. S. (1967). *J. Chem. Phys. 46*, 3437.

Bykova, E., et al. (2016). *Nat. Commun.*, *7*, 10661.

Cerantola, V., et al. (2017). *Nat. Commun.*, *8*, 15960.

Chau, R., Hamel, S., & Nellis, W. J. (2011). *Nat. Commun.*, *2*, 1198.

Chelazzi, D., Ceppatelli, M., Santoro, M., Bini, R., & Schettino, V. (2004). *Nat. Mater.*, *3*, 470.

Ciabini, L., Santoro, M., Gorelli, F. A., Bini, R., Schettino, V., & Raugei, S. (2007). *Nat. Mater.*, *6*, 39.

Clark, R. J. H., & Hester, R. E. *Spectroscopy of advanced materials*. Chichester: Wiley, Advances in Spectroscopy, 19.

Correa, A. A., Bonev, S. A., & Galli, G. (2006). *Proc. Natl. Acad. Sci. U.S.A.*, *103*, 1204.

De Corte, K., Korsakov, A., Taylor, W. R., Cartigny, P., Ader, M., & De Paepe, P. (2000). *Isl. Arc*, *9*, 428.

Drickamer, H. G. (1967). *Science*, *156*, 1183.

Eggert, J. H., Hicks, D. G., Celliers, P. M., Bradley, D. K., McWilliams, R. S., Jeanloz, R., Miller, J. E., Boehly, T. R., & Collins, G. W. (2009). *Nat. Phys.*, *6*, 40.

Erskine, D. J., & Nellis, W. J. (1991). *Nature*, *349*, 317.

Ferrari, A. C. (2002). *Diamond Relat. Mater.*, *11*, 1053.

Field, J. E. (1992). *The properties of natural and synthetic diamond*. San Diego: Academic Press.

Fitzgibbons, T. C., Guthrie, M., Xu, E. S., Crespi, V. H., Davidowski, S. K., Cody, G. D., Alem, N., & Badding, J. V. (2015). *Nat. Mater.*, *14*, 43.

Frondel, C., & Marvin, U. B. (1967). *Nature*, *214*, 587.

Gao, G. Y., Oganov, A. R., Ma, Y. M., Wang, H., Li, P. F., Li, Y. W., Iitaka, T., & Zou, G. T. (2010). *J. Chem. Phys.*, *133*, 144508.

Ghiringhelli, L. M., Los, J. H., Meijer, E. J., Fasolino, A., & Frenkel, D. (2004). *Phys. Rev. B*, *69*, 100101.

Gloahec, M. (2007). *Nat. Mater.*, *6*, 274.

Goncharov, A. F. (1987). *Sov. Phys. Uspekhi*, *30*, 525.

Goncharov, A. F., Makarenko, I. N., & Stishov, S. M. (1989). *Zh. Eksper. Teor. Fiziki*, *96*, 670.

Gauthier, M. et al. (2014). *Rev. Sci. Instrum.*, *85*, 11E616.

Goncharov, A. F., Makarenko, I. N., & Stishov, S. M. (1990). *High Pressure Res.*, *4*, 345.

Gupta, Y. M., Turneaure, S. J., Perkins, K., Zimmerman, K., Arganbright, N., Shen, G., and Chow, P. (2012). *Rev. Sci. Instrum.*, *83*, 123905.

Hanneman, R. E., Strong, H. M., & Bundy, F. P. (1967). *Science*, *155*, 995.

Hazen, R. M., Downs, R. T., Jones, A. P., & Kah, L. (2013). *Rev. Mineral. Geochem.*, *75*, 7.

Hemley, R. J., & Dera, P. (2000). *Rev. Mineral. Geochem.*, *41*, 335.

Hirai, H., Konagai, K., Kawamura, T., Yamamoto, Y., & Yagi, T. (2009). *Phys. Earth Planet. Inter.*, *174*, 242.

Hu, M. et al. (2017). *Sci. Adv.*, *3*, e1603213.

Hubbard, W. B. (1981). *Science*, *214*, 145.

Hwang, S. L., Shen, P., Chu, H. T., Yui, T. F., & Lin, C. C. (2001). *Earth Planet. Sci. Lett.*, *188*, 9.

Kenney, J. F., Kutcherov, V. A., Bendeliani, N. A., & Alekseev, V. A. (2002). *Proc. Natl. Acad. Sci. U.S.A.*, *99*, 10976.

Khaliullin, R. Z., Eshet, H., Kühne, T. D., Behler, J., & Parrinello, M. (2011). *Nat. Mater.*, *10*, 693.

Knudson, M. D., Desjarlais, M. P., & Dolan, D. H. (2008). *Science*, *322*, 1822.

Kolesnikov, A., Kutcherov, V. G., & Goncharov, A. F. (2009). *Nature Geosci.*, *2*, 566.

Kopylova, M., Navon, O., Dubrovinsky, L., & Khachatryan, (2010). *G. Earth Planet. Sci. Lett.*, *291*, 126.

Korsakov, A. V., Perraki, M., Zedgenizov, D. A., Bindi, L., Vandenabeele, P., Suzuki, A., & Kagi, H. (2010). *J. Petrol.*, *51*, 763.

Kraus, D., et al. (2016). *Nat. Commun.*, *7*, 10970.

Kraus, D., et al. (2017). *Nat. Astron.*, *1*, 606.

Lee, M. S., & Scandolo, S. (2011). *Nat. Commun.*, *2*, 1184.

Li, Q., Ma, Y., Oganov, A. R., Wang, H., Wang, H., Xu, Y., Cui, T., Mao, H.-K., & Zou, G. T. (2009). *Phys. Rev. Lett.*, *102*, 175506.

Lin, Y., Zhang, L., Mao, H.-K., Chow, P., Xiao, Y., Baldini, M., Shu, J., & Mao, W. L. (2011). *Phys. Rev. Lett.*, *107*, 175504.

Lobanov, S. S., et al. (2017). *Phys. Rev. B*, *96*, 104101.

Lobanov, S. S., Chen, P. N., Chen, X. J., Zha, C. S., Litasov, K. D., Mao, H. K., & Goncharov A. F., (2013). *Nature Comm.*, *4*, 2446.
Mao W. L., et al. (2003). *Science*, *302*, 425.
Martinez-Canales, M., Pickard, C. J., & Needs, R. J. (2012). *Phys. Rev. Lett.*, *108*, 045704.
Massonne, H. J. (2003). *Earth Planet. Sci. Lett.*, *216*, 347.
Merlini, M., Cerantola, V., Gatta, G. D., Gemmi, M., Hanfland, M., Kupenko, I., Lotti, P., Muller, H., & Zhang, L. (2017). *Am. Mineral.*, *102*, 1763.
Merlini, M., Hanfland, M., Salamat, A., Petitgirard, S., & Muller, H. (2015). *Am. Mineral.*, *100*, 2001.
Mikhailenko, D. S., Korsakov, A. V., Zelenovskiy, P. S., & Golovin, A. V. (2016). *Am. Mineral.*, *101*, 2155.
Miller, E. D., Nesting, D. C., & Badding, J. V. (1997). *Chem. Mater.*, *9*, 18.
Mundy, C. J., Curioni, A., Goldman, N., Will Kuo, I. F., Reed, E. J., Fried, L. E., & Ianuzzi, M. (2008). *J. Chem. Phys.*, *128*, 184701.
Németh, P., Garvie, L. A. J., Aoki, T., Dubrovinskaia, N., Dubrovinsky, L., & Buseck, P. R. (2014). *Nat. Commun.*, *5*, 5447.
Nestola, F., et al. (2018). *Nature*, *555*, 237.
Oganov, A. R., Glass, C. W., & Ono, S. (2006). *Earth Planet. Sci. Lett.*, *241*, 95.
Oganov, A. R., Hemley, R. J., Hazen, R. M., & Jones, A. P. (2013). *Rev. Mineral. Geochem.*, *75*, 47.
Oganov, A. R., Ono, S., Ma, Y. M., Glass, C. W., & Garcia, A. (2008). *Earth Planet. Sci. Lett.*, *273*, 38.
Ono, S., Kikegawa, T., & Ohishi, Y. (2007). *Am. Mineral.*, *92*, 1246.
Panero, W. R., & Kabbes, J. E. (2008). *Geophys. Res. Lett.*, *35*, L14307.
Pearson, D. G., et al. (2014). *Nature*, *507*, 221.
Pickard, C. J., & Needs, R. J. (2015). *Phys. Rev. B*, *91*, 104101.
Pineau, N. (2013). *J. Chem. Phys. C*, *117*, 12778.
Powles, R. C., Marks, N. A., Lau, D. W. M., McCulloch, D. G., & McKenzie, D. R. (2013). *Carbon*, *63*, 416.
Prewitt, C. T., & Downs, R. T. (1998). *Rev. Mineral. Geochem.*, 37, *283* (1998).
Pruzan, P., Chervin, J. C., Thiery, M. M., Itie, J. P., Besson, J. M., Forgerit, J. P., & Revault, M. (1990). *J. Chem. Phys.*, *92*, 6910.
Rygg, J. R., et al. (2012). *Rev. Sci. Instrum.*, *83*, 113904.
Santoro, M., Ciabini, L., Bini, R., & Schettino, V. (2003). *J. Raman Spectrosc.*, *34*, 557.
Schettino, V., & Bini, R. (2007). *Chem. Soc. Rev.*, *36*, 869.
Shchepetova, O. V., Korsakov, A., Mikhailenko, D., Zelenovskiy, P., Shur, V., & Ohfuji, H. (2017). *J. Raman Spectrosc.*, *48*, 1606.
Sherman, B. L., Wilson, H. F., Weeraratne, D., & Militzer, B. (2012). *Phys. Rev. B*, *86*, 224113.
Shi, X., He, C. R., Pickard, C. J., Tang, C. C., & Zhong, J. (2018). *Phys. Rev. B*, *97*, 014104.
Shiell, T. B., McCulloch, D. G., Bradby, J. E., Haberl, B., Boehler, R., & McKenzie, D. R. (2016). *Sci. Rep.*, *6*, 37232.
Skorodumova, N. V., Belonoshko, A. B., Huang, L., Ahuja, R., & Johansson, B. (2005). *Am. Mineral.*, *90*, 1008.
Smith, E. M., Shirey, S. B., Nestola, F., Bullock, E. S., Wang, J. H., Richardson, S. H., & Wang, W. Y. (2016). *Science*, *354*, 1403.
Smith, R. F., et al. (2014). *Nature*, *511*, 330.
Solomatova, N. V., & Asimow, P. D. (2017). *Am. Mineral.*, *102*, 210.
Spanu, L., Donadio, D., Hohl, D., Schwegler, E., & Galli, G. (2011). *Proc. Natl. Acad. Sci. U.S.A.*, *108*, 6843.
Stanley, S., & Bloxham, J., (2004). *Nature*, *428*, 151.
Tschauner, O., et al. (2018). *Science*, *359*, 1136.
Turneaure, S. J., Sharma, S. M., Volz, T. J., Winey, J. M., & Gupta, Y. M. (2017). *Sci. Adv.*, *3*, eaao3561.
Utsumi, W., & Yagi, T. (1991). *Science*, *252*, 1542.
Vennari, C. E., & Williams, Q. (2018). *Am. Mineral.*, *103*, 171.
Wang, X., Scandolo, S., & Car, R. (2005). *Phys. Rev. Lett.*, *95*, 185701.
Wang, Y., Panzik, J. E., Kiefer, B., & Lee, K. K. M. (2012). *Sci. Rep.*, *2*, 520.
Wang, Z., et al. (2004). *Proc. Natl. Acad. Sci. U.S.A.*, *101*, 13699.
Wen, X. D., Hoffmann, R., & Ashcroft, N. W. (2011). *J. Am. Chem. Soc.*, *133*, 9023.
Wirth, R., Dobrzhinetskaya, L., Harte, B., Schreiber, A., & Green, H. W. (2014). *Earth Planet. Sci. Lett.*, *404*, 365.
Xie, Y.-P., Zhang, X.-J., & Liu, Z.-P. (2017). *J. Am. Chem. Soc.*, *139*, 2545.
Xu, J., Mao, H.-K., & Hemley, R. J. (2002). *J. Phys.: Cond. Mater.*, *14*, 11549.
Yao, X., Xie, C., Dong, X., Oganov, A. R., & Zeng, Q. F. (2018). *Phys. Rev. B*, *98*, 014108.
Yin, M. T., & Cohen, M. L. (1983). *Phys. Rev. Lett.*, *50*, 2006.
Zeng, Z., et al. (2017). *Nat. Commun.*, *8*, 322.
Zhang, C., & Duan, Z. H. (2009). *Geochim. Cosmochim. Acta*, *73*, 2089.